ACS NANO

www.acsnano.org

ARTICLE

Cerium Oxide Nanocrystal Embedded Bimodal Micromesoporous Nitrogen-Rich Carbon Nanospheres as Effective Sulfur Host for Lithium–Sulfur Batteries

Lianbo Ma,[†] Renpeng Chen,[†] Guoyin Zhu,[†] Yi Hu,[†] Yanrong Wang,[†] Tao Chen,[†] Jie Liu,[†,‡] and Zhong Jin*[,†]

[†]Key Laboratory of Mesoscopic Chemistry of MOE and Collaborative Innovation Center of Chemistry for Life Sciences, School of Chemistry and Chemical Engineering, Nanjing University, Nanjing, Jiangsu 210093, China

[‡]Department of Chemistry, Duke University, Durham, North Carolina 27708, United States

Supporting Information

ABSTRACT: For developing lithium–sulfur (Li–S) batteries, it is critical to design advanced cathode materials with high sulfur loading/utilization ratios and strong binding interactions with sulfur species to prevent the dissolution of intermediate polysulfides. Here we report an effective sulfur host material prepared by implanting cerium oxide (CeO_2) nanocrystals homogeneously into well-designed bimodal micromesoporous nitrogen-rich carbon (MMNC) nanospheres. With the high conductivity and abundant hierarchical pore structures, MMNC nanospheres can effectively store and entrap sulfur species. Moreover, the inserted polar and electrocatalytically active CeO_2 nanocrystals and high nitrogen content of MMNC can synergistically solve the hurdle of the polysulfide dissolution and furthermore significantly promote stable redox activity. By combining these advantages, CeO_2/MMNC-S cathodes with 1.4 mg cm^{-2} sulfur exhibit high reversible capacities (1066 mAh g^{-1} at 0.2 C after 200 cycles and 836 mAh g^{-1} at 1.0 C after 500 cycles), good rate capability (737 mAh g^{-1} at 2.0 C), and high cycle stability (721 mAh g^{-1} at 2.0 C after 1000 cycles with a low capacity decay of 0.024% per cycle). Furthermore, a high and stable reversible capacity of 611 mAh g^{-1} is achieved after cycling for 200 cycles with higher sulfur loading of 3.4 mg cm^{-2}.

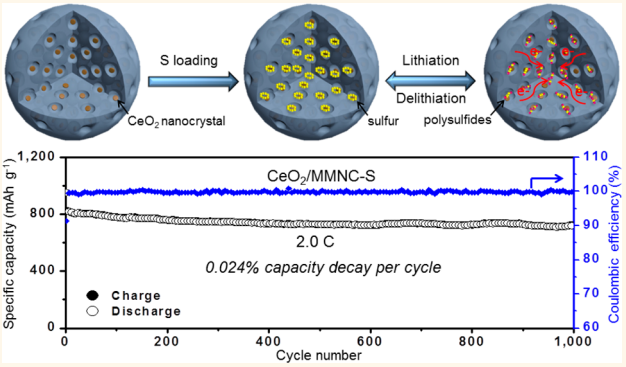

KEYWORDS: *Li–S batteries, cerium oxide, micromesoporous nitrogen-rich carbon nanospheres, physical and chemical confinement, shuttle effect*

The rapidly growing demand of portable electronics and electric vehicles has stimulated intensive research on advanced electrochemical energy storage techniques.[1−5] Among the next-generation batteries that promise to replace lithium-ion batteries (LIBs), lithium–sulfur (Li–S) batteries are very attractive due to the superior theoretical specific capacity (1675 mAh g^{-1}) and energy density (2600 Wh kg^{-1}).[6−8] However, the commercialization of Li–S batteries is seriously hindered by the low sulfur utilization and the rapid capacity fading resulted from the poor electrical conductivity of sulfur, the high solubility of intermediate polysulfides, and the large volumetric expansion upon the full transformation of sulfur to Li_2S.[9−12] To resolve these problems, great efforts have been devoted on the design and construction of micro/nanostructured sulfur host materials.

Carbon nanomaterials with high conductivity and accessible porosity (such as carbon nanotubes,[13] carbon nanocages,[14] porous carbon,[15] graphene,[16] and carbon fibers[17]) have been widely used for the construction of sulfur/carbon composites to improve the conductivity of sulfur cathode and alleviate the dissolution of intermediate polysulfides. Nanostructured carbons can provide large pore volume for sulfur storage and also facilitate the access of electrolyte.[18] The chemical modifications of carbon materials by heteroatom substitution have also shown some potential for the confinement of lithium polysulfides.[19−21] However, owing to the relatively weak

Received: May 9, 2017
Accepted: July 6, 2017
Published: July 6, 2017

DOI: 10.1021/acsnano.7b03227
ACS Nano 2017, 11, 7274–7283

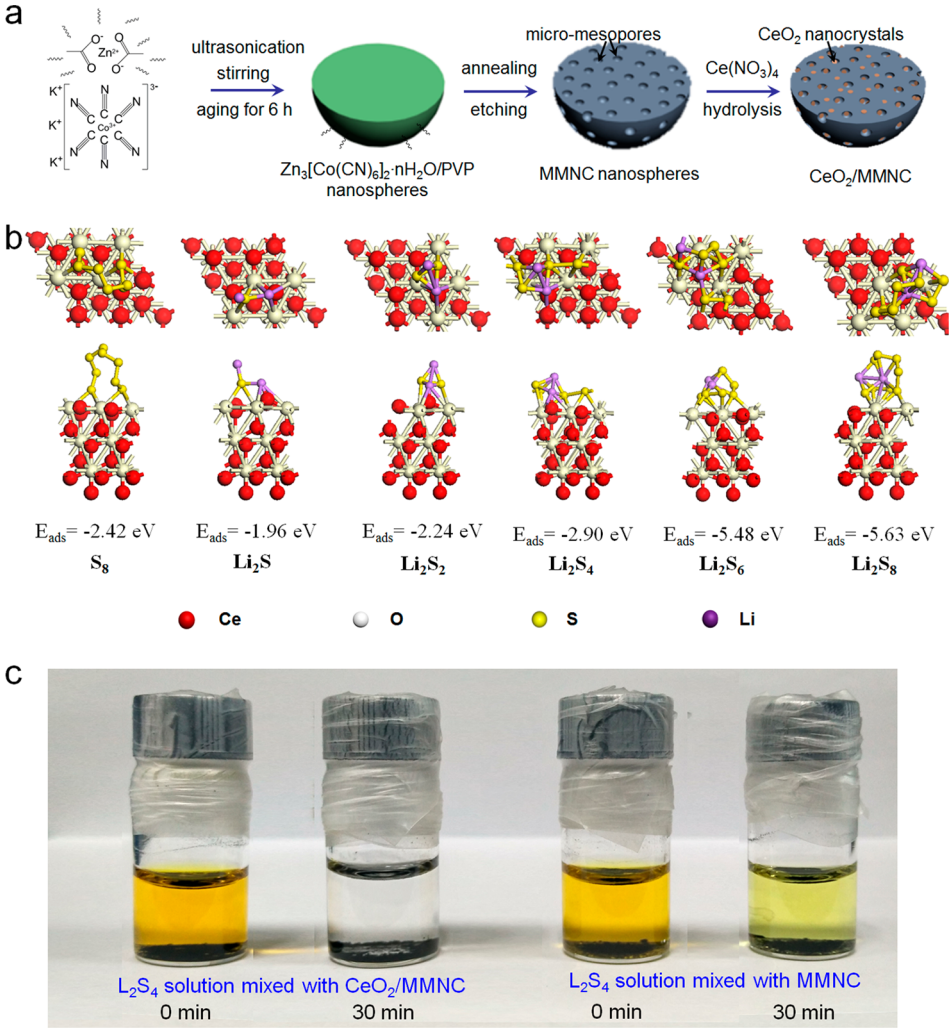

Figure 1. Synthesis process, theoretical simulations, and polysulfide adsorption ability of CeO_2/MMNC material. (a) Schematic synthesis procedure of CeO_2/MMNC nanospheres. (b) Binding geometric configurations and binding energies of S_8 and Li_2S_x species with the (111) planes of CeO_2 nanocrystals. The high binding energies indicate the strong interaction between lithium polysulfides and CeO_2 nanocrystals. (c) The adsorption ability comparison of CeO_2/MMNC and MMNC host materials with Li_2S_4 as the representative polysulfide. The Li_2S_4 solution mixed with CeO_2/MMNC material shows obvious discoloration in only 30 min, suggesting the high adsorption ability of CeO_2/MMNC.

interaction between the almost nonpolar carbon materials and polar lithium polysulfides, the physical confinement in nanocarbons still suffers from the leakage of lithium polysulfides and results in capacity fading over cycling.[22,23]

Recently, polar materials, such as transition-metal oxides,[24,25] sulfides,[26,27] and metal−organic frameworks (MOFs),[28,29] have been reported as sulfur hosts to improve the adsorption of intermediate polysulfides. Different from carbon materials, the strong interaction between polar species and lithium polysulfides was considered as the key reason for the effective confinement of polysulfides.[30] However, these polar sulfur hosts usually are restricted by poor electrical conductivity, which undoubtedly limits the full utilization of sulfur. The design of hybrid nanostructures that combine the advantages of nanocarbons and polar materials has been considered as a promising solution for the construction of advanced sulfur composite cathodes.[31−34] Currently, carbon/polar material hybrids, such as carbon nanotubes/V_2O_5,[35] nitrogen-doped graphene/TiO_2,[36] carbon cloth/Al_2O_3,[37] and hollow carbon fibers/MnO_2,[38] have attracted extensive attention as the representative state-of-the-art sulfur hosts in Li−S batteries. The carbon frameworks can allow the high sulfur loadings, improve the overall electrical conductivity, and serve as the porous container for the storage of sulfur species, and polar materials can provide strong chemical affinity with sulfur species and block the dissolution of soluble polysulfides during discharge.

Herein, we demonstrate a design of sulfur host by implanting CeO_2 nanocrystals homogeneously in the hierarchical pores of bimodal micromesoporous nitrogen-rich carbon nanospheres (CeO_2/MMNC) for the effective confinement of sulfur species. The CeO_2/MMNC hybrid material has ample micromesopores, abundant polar absorption sites, three-dimensional nanochannels, and good electrical conductivity that can take full advantage of combining both physical and chemical interactions with lithium polysulfides. More importantly, the CeO_2 nanocrystals with high electrocatalytic activity can significantly promote the polysulfide redox reactions. As a result, the CeO_2/MMNC-S cathodes exhibit high reversible capacity, great rate performance, and remarkable cycle stability compared to previously reported representative sulfur host materials (Table S1).

DOI: 10.1021/acsnano.7b03227
ACS Nano 2017, 11, 7274−7283

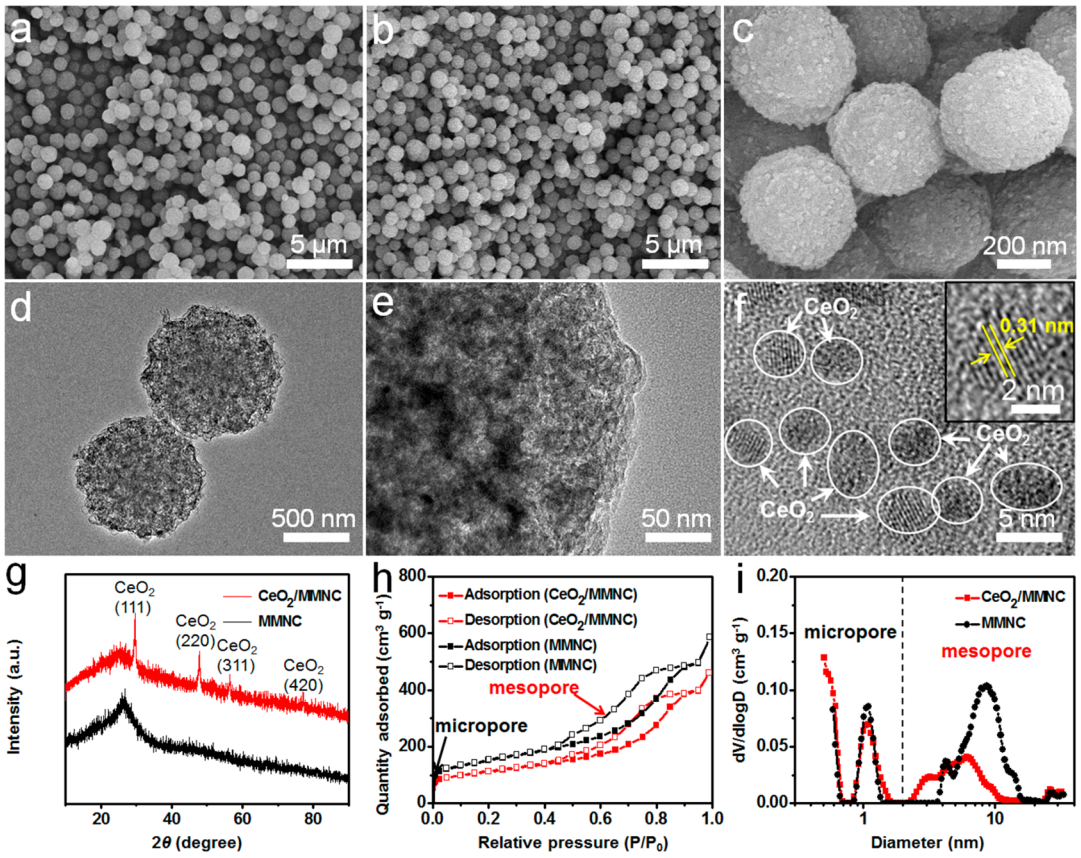

Figure 2. Morphological and structural characterizations of MMNC and CeO_2/MMNC nanospheres. (a) SEM image of MMNC nanospheres. (b,c) SEM and (d–f) TEM images of CeO_2/MMNC nanospheres. (f) HRTEM image of CeO_2 nanocrystals embedded in the pores of MMNC nanospheres. The lattice distance in the inset of (f) is 0.31 nm, corresponding to the (111) planes of CeO_2 nanocrystals. (g) XRD patterns, (h) N_2 adsorption–desorption isotherms, and (i) pore size distributions of MMNC and CeO_2/MMNC, respectively.

RESULTS AND DISCUSSION

The process for preparing CeO_2/MMNC host material is schematically illustrated in Figure 1a. First, $Zn_3[Co(CN)_6]_2 \cdot nH_2O$/polyvinylpyrrolidone (PVP) precursor nanospheres were synthesized by an ultrasonication method, as detailed in the Experimental Section. X-ray diffraction (XRD) of the precursor nanospheres (Figure S1) reveals that all diffraction peaks can be attributed to cubic-phase $Zn_3[Co(CN)_6]_2 \cdot nH_2O$ (JCPDS card, no. 23-1494, space group: $Fm\bar{3}m$, a = 9.940, b = 9.940, c = 9.940). A scanning electron microscopy (SEM) image of the precursor nanospheres (Figure S2) shows a uniform spherical morphology with an average size of ~600 nm. After thermal annealing and acidic etching, the precursor nanospheres were converted into MMNC nanospheres, meanwhile abundant micropores and mesopores were formed, which is conducive to the encapsulation and storage of sulfur species. To further improve the adsorption and confinement of intermediate polysulfides, CeO_2 nanocrystals were embedded into MMNC nanospheres (Figure 1a). Theoretical simulations were performed to verify the strong interaction between the CeO_2 nanocrystals and polysulfides (Figure 1b). Moreover, the (111) surface of CeO_2 was selected due to the least surface energy and behavior as the most stable structure. Figure S3 shows the optimized structures of S_8 and Li_2S_x species, which exhibit three-dimensional cluster shapes. The binding energies between CeO_2 nanocrystals with S_8, Li_2S, Li_2S_2, Li_2S_4, Li_2S_6, or Li_2S_8 species are −2.42, −1.96, −2.24, −2.90, −5.48, or −5.63 eV, respectively. These values are much higher than those of pristine MMNC (Figure S4) and also comparable or superior to those of other polar materials,[39−42] indicating the strong chemical interactions between CeO_2 nanocrystals and sulfur species. To compare the polysulfide adsorption behaviors of CeO_2/MMNC and pristine MMNC, 10 mg of these samples were separately added into 2.0 mL of 0.005 M L_2S_4 solution in a mixed solvent of dimethoxyethane/dioxolane (DME/DOL, with a volume ratio of 1:1) (Figure 1c). The Li_2S_4 solution mixed with CeO_2/MMNC shows much more obvious discoloration than that mixed with pristine MMNC, consistent with the above theoretical predictions. To give more insights on the improved adsorption of CeO_2/MMNC material, cyclic voltammetry (CV) and X-ray photoelectron spectroscopy (XPS) were conducted. As shown in Figure S5a, the CeO_2 nanocrystals have a redox potential of 2.72 V *vs* Li/Li^+, which is higher than that of polysulfides (2.10 V *vs* Li/Li^+), indicating that the CeO_2 nanocrystals can oxidize the intermediate polysulfides to thiosulfates and polythionates.[43] Moreover, the high-resolution XPS spectrum after the adsorption tests (Figure S5b) shows four binding energies related to different sulfur species: "bridging" sulfur species (S_B, 163.3 and 162.4 eV), "terminal" sulfur species (S_T, 165.0 and 163.8 eV), thiosulfates (168.0 and 167.2 eV), and polythionates (169.8 and 168.7 eV).[43] The thiosulfates and polythionates are mainly originated from the oxidation of intermediate polysulfides by incorporated CeO_2 nanocrystals[43] and can act as a surface-bound active redox mediator to yield a very low capacity fade rate during charge/discharge processes.

DOI: 10.1021/acsnano.7b03227
ACS Nano 2017, 11, 7274–7283

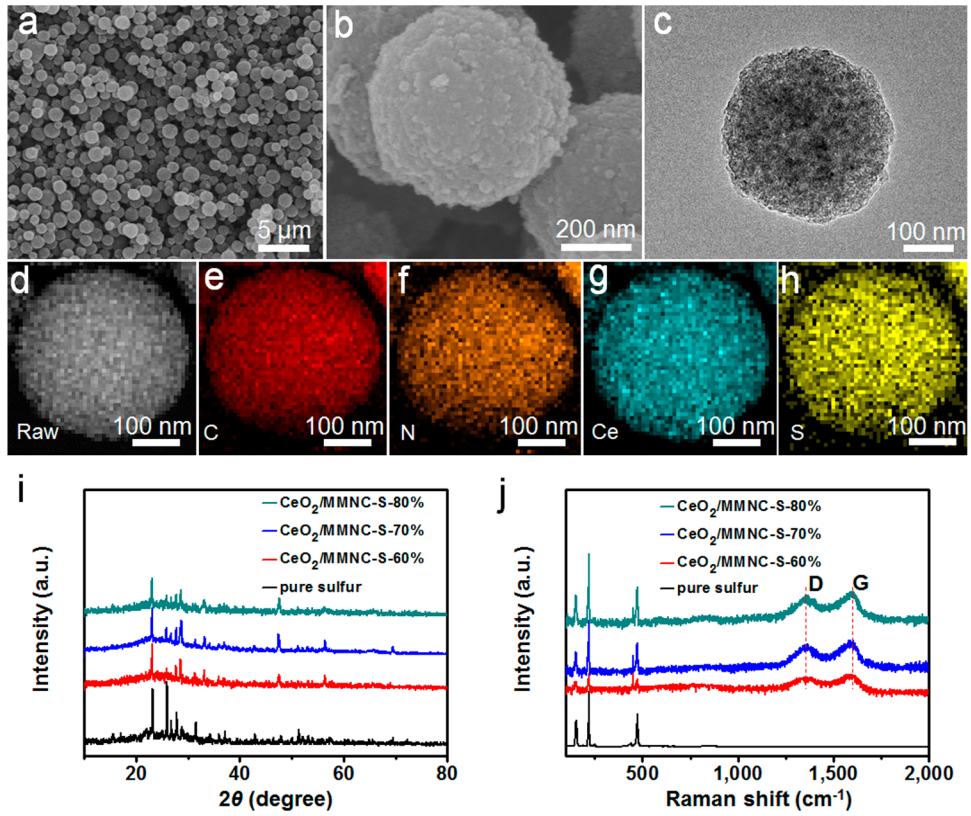

Figure 3. Morphology and composition characterizations of CeO_2/MMNC-S-*x* composites. (a,b) SEM and (c) TEM images of CeO_2/MMNC-S-70%. (d) STEM image and (e−h) corresponding EFTEM elemental mapping (C, N, Ce, and S elements) of CeO_2/MMNC-S-70%, respectively. (i) XRD patterns and (j) Raman spectra of CeO_2/MMNC-S-*x* composites and pure sulfur, respectively.

The morphological and structural characterizations of as-prepared MMNC nanospheres are shown in Figure 2. The MMNC nanospheres have an average size of ~500 nm, slightly smaller than the precursor nanospheres (~600 nm) owing to the volume shrinkage during carbonization process. SEM images (Figure 2b,c) reveal the spherical shape and uniform size distribution of CeO_2/MMNC nanospheres. Transmission electron microscopy (TEM) images show that all CeO_2 nanocrystals are embedded in the pores of MMNC nanospheres rather than attached on the surface (Figure 2d−f). The high-resolution TEM (HRTEM, Figure 2f) image demonstrates almost the layered structure of CeO_2 nanocrystals, consistent with the crystalline structure reported in the literature.[44] Moreover, CeO_2 nanocrystals with a size distribution of 3−5 nm are homogeneously distributed inside the MMNC nanospheres. The inset of Figure 2f reveals an interlayer distance of 0.31 nm, corresponding to the (111) planes of CeO_2 nanocrystals.

The XRD pattern of MMNC (Figure 2g) shows a broad diffraction peak cantered at ~26°, corresponding to the (002) planes of graphite, while the XRD pattern of CeO_2/MMNC shows four additional conspicuous peaks ascribed to the CeO_2 nanocrystals (JCPDS card, no. 34-0394, space group: $Fm\bar{3}m$, a = 5.411, b = 5.411, c = 5.411). Raman spectrum of MMNC (Figure S6) displays typical features of porous carbon, and the intensity ratio of D and G bands (I_D/I_G = 0.92) indicates the partially graphitic nature. The Raman spectrum of CeO_2/MMNC shows an additional peak at ~458 cm^{-1}, attributed to the F_{2g} mode of CeO_2.[45] The specific surface area and porous characteristics of MMNC and CeO_2/MMNC were investigated by N_2 adsorption−desorption isotherms (Figure 2h), revealing Brunauer−Emmer−Teller (BET) surface areas of *ca.* 550 and 435 $m^2\ g^{-1}$, respectively. The pore size distributions in Figure 2i demonstrate the bimodal micromesoporous structures in both MMNC and CeO_2/MMNC materials. For MMNC nanospheres, the diameter of micropores is centered at ~1.1 nm, and the diameter of mesopores falls into the range of 3−12 nm. While for CeO_2/MMNC material, the size of mesopores is slightly smaller (around 2−10 nm), owing to the encapsulation of CeO_2 nanocrystals.

The survey XPS spectrum of CeO_2/MMNC material (Figure S7) suggests the coexistence of C, N, Ce, and O elements. The weight contents of N and Ce were measured to be *ca.* 8.4 and 15.6 wt %, respectively. The high-resolution XPS spectrum at N 1s region (Figure S8a) can be deconvoluted into three peaks, corresponding to the pyridinic N (N-6, 398.4 ± 0.2 eV), pyrrolic N (N-5, 399.8 ± 0.2 eV), and graphitic N (N-G, 400.7 ± 0.2 eV), respectively.[46] The nitrogen species (especially N-6 and N-5) in porous carbons are helpful to trap intermediate polysulfides and alleviate the dissolution process upon charging/discharging.[47,48] The high-resolution XPS spectrum at Ce 3d region (Figure S8b) shows six deconvoluted peaks originated from the CeO_2 nanocrystals.[49]

To construct the cathode materials of Li−S batteries, a practicable approach to infiltrate sulfur into carbon/polar material hybrids would be the melt-diffusion strategy, owing to the simple, convenient, and effective operation proccess.[50] By controlling the amount of sulfur in the mixture, the samples of CeO_2/MMNC-S-*x* (x = 60%, 70%, or 80%) composites were prepared, where x stands for the starting weight percentage of sulfur added in the mixture. The SEM (Figure 3a,b) and TEM images (Figure 3c) of CeO_2/MMNC-S-70% are comparable to

DOI: 10.1021/acsnano.7b03227
ACS Nano 2017, 11, 7274−7283

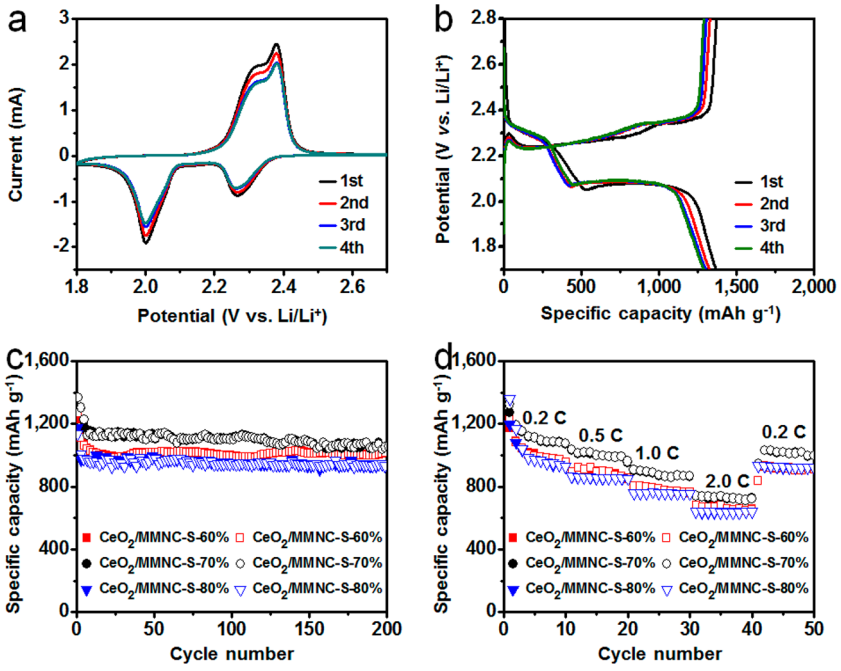

Figure 4. Electrochemical performances of CeO_2/MMNC-S-*x* composites as cathode materials in Li−S batteries with 1.4 mg cm^{-2} sulfur. (a) CV curves of CeO_2/MMNC-S-70% cathode at a scan rate of 0.2 mV s^{-1}. (b) Galvanostatic charge/discharge profiles of CeO_2/MMNC-S-70% cathode at 0.2 C. (c) Cycling performances of CeO_2/MMNC-S-*x* cathodes at 0.2 C. (d) Rate capabilities of CeO_2/MMNC-S-*x* cathodes.

those of pristine CeO_2/MMNC, and no sulfur particles are observed on the surface. The scanning TEM (STEM) image (Figure 3d) and elemental mapping by energy-filtered TEM (EFTEM) (Figure 3e−h) demonstrate the coexistence and uniform distribution of C, N, Ce, and S elements, suggesting that sulfur is homogeneously filled in the pores. The XRD patterns (Figure 3i) and Raman spectra (Figure 3j) of CeO_2/MMNC-S-*x* composites exhibit the characteristic peaks of porous carbon, CeO_2 nanocrystals, and sulfur. The accurate sulfur contents in CeO_2/MMNC-S-60%, CeO_2/MMNC-S-70%, and CeO_2/MMNC-S-80% measured by thermogravimetric analysis (TGA, Figure S9) are 56.5, 63.6, and 68.3 wt %, respectively. Considering the unique structures and special compositions of CeO_2/MMNC hybrids, the achieved sulfur loading masses are acceptable, and moreover, these values are comparable to the previously reported carbon/polar material hybrids summarized in Table S1.

As control experiments, pristine MMNC nanospheres filled with sulfur were also employed as sulfur host material, denoted as MMNC-S-*x* (*x* = 60%, 70%, or 80%, where *x* represents the initial weight percentage of sulfur). The morphology and composition characterizations of MMNC-S-70% composites are shown in Figure S10, indicating the successful encapsulation of sulfur. The sulfur contents of MMNC-S-60%, MMNC-S-70%, and MMNC-S-80% composites determined by TGA are 58.4, 68.6, and 77.8 wt %, respectively (Figure S11).

The electrochemical performances of CeO_2/MMNC-S-*x* composites for Li−S batteries were investigated, and the sulfur loading mass was about 1.4 mg cm^{-2}. The CV curves of CeO_2/MMNC-S-70% cathode at 0.2 mV s^{-1} show two distinctive reduction peaks appear at 2.27 and 2.01 V (Figure 4a). The broad reduction peak at 2.27 V is attributed to the reduction of S_8 to intermediate polysulfides (Li_2S_x, $4 \le x \le 8$), while the second reduction peak at 2.01 V is ascribed to the further reduction of intermediate polysulfides to insoluble Li_2S or Li_2S_2.[51,52] A strong oxidation peak centered at 2.38 V corresponds to the delithiation processes from Li_2S/Li_2S_2 to Li_2S_x and eventually to S_8.[53] In the following cycles, the intensities of reduction and oxidation peaks remain almost unchanged, while the reduction peaks shift to slightly higher potentials of 2.29 and 2.03 V, respectively, suggesting a decreased polarization after the first activation cycle. Moreover, as revealed in Figure S12, the CV curve of CeO_2/MMNC-S-70% composite cathode shows a distinguishable positive shift in the reduction peaks, negative shift in the oxidation peaks, and higher peak current densities as compared with those of MMNC-S-70% composite cathode, indicating the strong electrocatalytic effect and improved polysulfide redox kinetics resulted from CeO_2 nanocrystals.[54] This conclusion is similar to the recent studies on Nb_2O_5,[31] MnO_2,[38,55] Ti_4O_{11},[56] and VN[57] materials. The typical charge/discharge profiles of CeO_2/MMNC-S-70% cathode within the potential range of 1.7−2.8 V *vs* Li/Li^+ at the current density of 0.2 C are displayed in Figure 4b. In the initial cycle, two potential plateaus are presented in the discharge process, while one potential plateau is observed in the charge process. The charge/discharge profiles of second, third, and fourth cycles show similar features and are well consistent with the CV curves (Figure 4a). The discharge capacity based on the loading weight of sulfur in the initial cycle is as high as 1368 mAh g^{-1}, suggesting the high utilization of sulfur. In the fourth cycle, the discharge capacity maintains at 1247 mAh g^{-1}, about 91.1% capacity retention of the initial cycle. The CV curves and charge/discharge profiles of CeO_2/MMNC-S-60% and CeO_2/MMNC-S-80% cathodes are presented in Figure S13, showing the electrochemical characteristics similar to those of CeO_2/MMNC-S-70%.

The cycling performances of CeO_2/MMNC-S-*x* at 0.2 C are presented in Figure 4c. CeO_2/MMNC-S-70% cathode exhibits the highest initial discharge and charge capacities (1368 and 1369 mAh g^{-1}, respectively). The discharge capacity gradually decreases to 1163 mAh g^{-1} at the sixth cycle, then keeps very stable and finally reaches 1066 mAh g^{-1} at the 200th cycle,

DOI: 10.1021/acsnano.7b03227
ACS Nano 2017, 11, 7274−7283

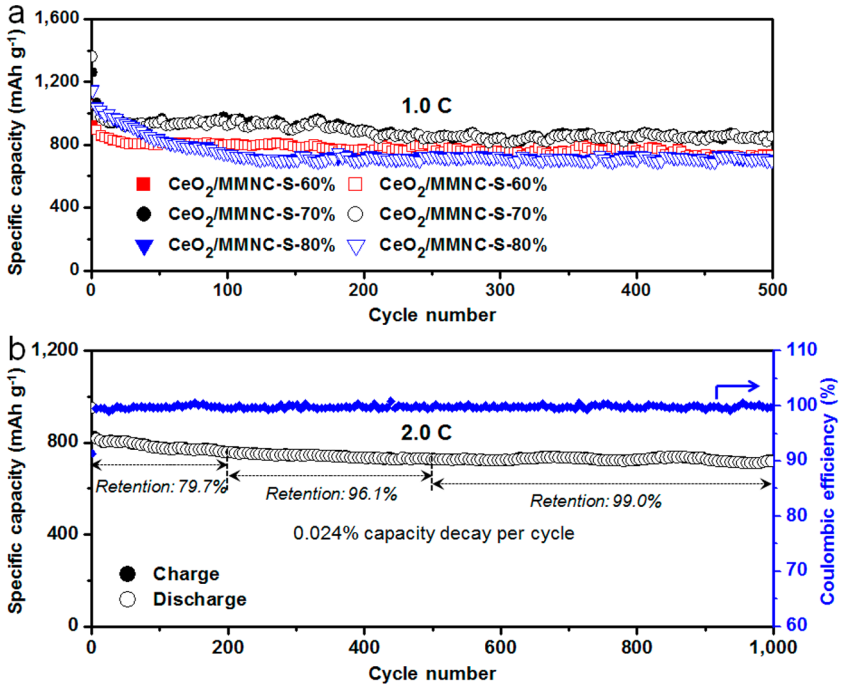

Figure 5. Long-term cycling stability of CeO_2/MMNC-S-*x* cathodes at high rates with 1.4 mg cm^{-2} sulfur. (a) Cycling tests of CeO_2/MMNC-S-*x* cathodes at 1.0 C. (b) Cycling test and corresponding Coulombic efficiency of CeO_2/MMNC-S-70% cathode at 2.0 C.

suggesting the high stability. The CeO_2/MMNC-S-60% and CeO_2/MMNC-S-80% cathodes deliver slightly lower discharge capacities of 1021 and 937 mAh g^{-1} after 200 cycles, respectively. As compared with other representative sulfur host materials (Table S1), CeO_2/MMNC-S-70% cathode shows remarkable electrochemical performances.

Figure 4d shows the rate performances of CeO_2/MMNC-S-*x* cathodes under various current rates. The CeO_2/MMNC-S-70% cathode shows the best rate capability, with discharge capacities of 1147, 1020, 877, and 737 mAh g^{-1} at 0.2, 0.5, 1.0, and 2.0 C respectively. When reset to 0.2 C, the discharge capacity recovers to 1014 mAh g^{-1}. The discharge capacities of CeO_2/MMNC-S-60% and CeO_2/MMNC-S-80% cathodes at 2.0 C are slightly lower (673 and 642 mAh g^{-1}, respectively). Electrochemical impedance spectroscopy (EIS) was also conducted, as shown in Figure S14, and the Nyquist plots demonstrate the good electrical conductivity of CeO_2/MMNC-S-*x* cathodes.

The life spans of CeO_2/MMNC-S-*x* cathodes were investigated under 1.0 and 2.0 C. As presented in Figure 5, the CeO_2/MMNC-S-70% cathode exhibits the highest cycling performance among CeO_2/MMNC-S-*x* cathodes at 1.0 C. The initial discharge capacity reaches 1352 mAh g^{-1}, then it decreases to 866 mAh g^{-1} at the 200th cycle and finally maintains at 836 mAh g^{-1} at the 500th cycle. The discharge capacities of CeO_2/MMNC-S-60% and CeO_2/MMNC-S-80% cathodes at 1.0 C after 500 cycles are 760 and 706 mAh g^{-1}, respectively. Further increasing to 2.0 C, the CeO_2/MMNC-S-70% composite still exhibits high capacity and extremely long cycle life with a low capacity decay of 0.024% per cycle over 1000 cycles. Remarkably, the discharge capacity of CeO_2/MMNC-S-70% reaches 721 mAh g^{-1} after 1000 cycles with the Coulombic efficiency of 99.7%, higher than previously reported sulfur cathode materials (Table S1). Moreover, the cycling performance of CeO_2/MMNC-S-70% composite cathode was also tested in the electrolyte without $LiNO_3$ additive (Figure S15). At 1.0 and 2.0 C, the CeO_2/MMNC-S-70% cathodes exhibit remarkable cycling stability with the discharge capacities of 953 and 772 mAh g^{-1} after cycling for 100 cycles, accompanied with the capacity retentions of 79.9% and 71.0%, respectively; moreover, the Coulombic efficiencies of CeO_2/MMNC-S-70% cathodes after 100 cycles keep at 99.6% and 99.2%, respectively, indicating that the shuttle effect has been well suppressed. These results confirm that the CeO_2/MMNC host can efficiently adsorb the polysulfides and suppress the shuttle effects even without the $LiNO_3$ additive, thus conducive to the long-term cycling performance. In addition, to investigate the structural integrity of CeO_2/MMNC during the charge/discharge processes, SEM images of CeO_2/MMNC-S-70% composite after cycling 1000 cycles at 2.0 C are provided in Figure S16. The spherical shape maintains well after the long-term testing, demonstrating the highly structural stability of CeO_2/MMNC material.

For comparison, the electrochemical performances of MMNC-S-*x* composites were also investigated. As shown in Figure S17, the CV curves and charge/discharge profiles display similar features to those of CeO_2/MMNC-S-*x* cathodes. The MMNC-S-70% cathode exhibits the best electrochemical performance among MMNC-S-*x* composites. After 100 cycles at 0.2 C, the discharge capacity reaches 833 mAh g^{-1} (Figure S17c), and the discharge capacity decreases to ~530 mAh g^{-1} at 2.0 C (Figure S17d). The MMNC-S-70% cathode delivers stable cycling performance with the lower discharge capacities of 670 mAh g^{-1} at 1.0 C after 500 cycles (Figure S18a) and 503 mAh g^{-1} at 2.0 C after 1000 cycles with 0.051% capacity decay per cycle (Figure S18b). All of these results demonstrate that the CeO_2/MMNC-S-70% cathode has better performance than that of the MMNC-S-70% cathode, attributed to the strong affinity and redox reactions of CeO_2 nanocrystals with intermediate polysulfides.

The electrochemical performance of CeO_2/MMNC-S cathode with high sulfur loading mass was also investigated.

DOI: 10.1021/acsnano.7b03227
ACS Nano 2017, 11, 7274−7283

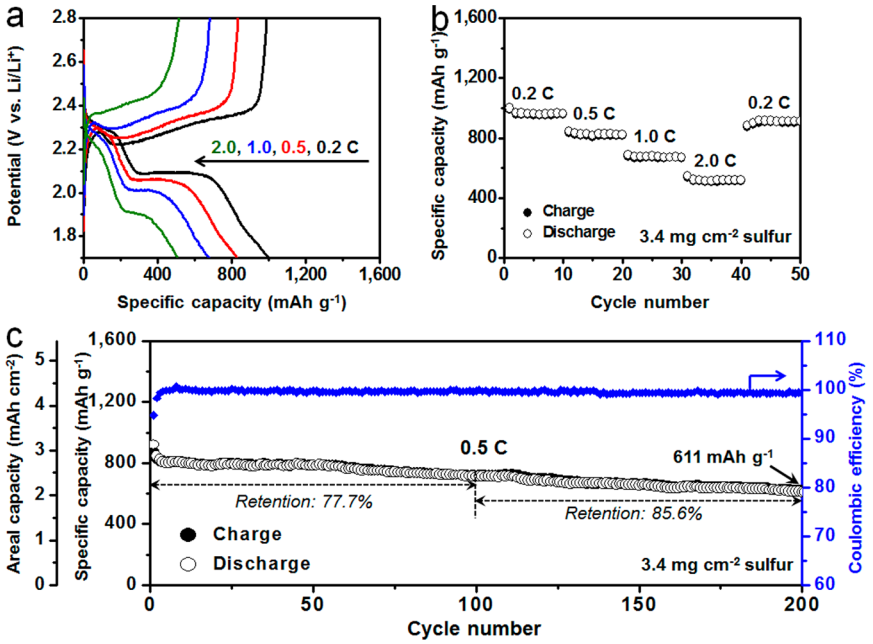

Figure 6. Electrochemical performance of CeO_2/MMNC-S-70% cathode with 3.4 mg cm^{-2} sulfur. (a) Charge/discharge profiles and (b) rate performance of CeO_2/MMNC-S-70% cathode under various rates. (c) Cycling performance of CeO_2/MMNC-S-70% cathode at 0.5 C.

As shown in Figure 6, the high sulfur loading electrode (3.4 mg cm^{-2}) shows slightly lower capacity than that of the electrode with 1.4 mg cm^{-2} due to a decreased interface between the electrolyte and sulfur with an increased thickness of the active material. However, the CeO_2/MMNC-S cathode still presents a high capacity with good cycling stability. Figure 6a displays the charge/discharge profiles of CeO_2/MMNC-S-70% cathode under various current rates. The charge/discharge profiles at high rates exhibit the similar profile characteristics to that at low current rates, and the capacity at 2.0 C can reach 520 mAh g^{-1} (Figure 6b). The cycling performance of CeO_2/MMNC-S-70% cathode at 0.5 C was also examined (Figure 6c). The initial discharge capacity is 920 mAh g^{-1} (3.13 mAh cm^{-2}), and after cycling for 200 cycles, the capacity remains 611 mAh g^{-1} (2.08 mAh cm^{-2}), corresponding to the capacity retention of 66.5%. In addition, to confirm the practical use toward Li−S batteries, the CeO_2/MMNC-S-70% cathode was then assembled into soft-packaged Li−S batteries with Li foil as anodes. As shown in Figure S19, the soft-packaged Li−S battery delivers a high initial capacity of 1056 mAh g^{-1}, and it can light the light-emitting-diode (LED), proving its potential for practical applications.

CONCLUSIONS

In summary, an optimized sulfur host material combining polar rare-earth metal oxide and bimodal micromesoporous carbon nanomaterials has been achieved. This hybrid structure benefits from both the physical confinement of the polysulfides by the mesoporous carbon microspheres and their chemical bindings to the CeO_2 nanocrystals and N-doped carbon species. More importantly, the CeO_2 nanocrystals can promote the chemical redox reactions of polysulfides, thus significantly enhancing their retentions upon cycling. The cathodes based on CeO_2/MMNC-S-*x* composites show high-energy capacity, good rate capability, and ultralong cycle life at both low and high sulfur loadings. The present work demonstrates the significant potential in practical application of high-energy density and long-life Li−S batteries.

EXPERIMENTAL SECTION

Chemicals. All the chemicals were purchased from Sinopharm Chemical Reagent Co., Ltd. with analytical grade and were used without further purification.

Preparation of MMNC Nanospheres. Typically, 0.60 mmol of zinc acetate dihydrate ($Zn(Ac)_2{\cdot}2H_2O$) and 0.40 g of polyvinylpyrrolidone (PVP) were dissolved in 20 mL of deionized water with ultrasonication to form a transparent solution. Then, 20 mL of potassium hexacyanocobaltate ($K_3[Co(CN)_6]$, 20 mmol L^{-1}) aqueous solution was slowly added into the above solution under ultrasonication and vigorous stirring at 0 °C. After aging for 6 h at room temperature, the precipitate of $Zn_3[Co(CN)_6]_2{\cdot}nH_2O$/PVP precursor nanospheres was collected by centrifugation, washed with deionized water for several times, and vacuum dried at 60 °C overnight. The precursor nanospheres were first thermal annealed at 600 °C for 2 h in N_2 atmosphere with a heating rate of 2 °C min^{-1} and then etched by hydrofluoric acid (HF, 5 wt %) and hydrochloric acid (HCl, 1.0 M) solution, successively. Finally, the product was collected by centrifugation, washed with deionized water and absolute ethanol for several times, and dried at 60 °C in a vacuum oven.

Synthesis of CeO_2/MMNC Nanospheres. In a typical procedure, 100 mg of MMNC nanospheres was dispersed into 100 mL of deionized water under vigorous stirring. Subsequently, 200 mg of $Ce(NO_3)_4$ was added into the above mixture and kept stirring for 6 h. The mixture was heated to 95 °C, and then 4 mL of 6-aminocaproic acid aqueous solution (125 mg/mL) and 20 μL of concentrated HCl (37 wt %) were introduced successively. Then, the resultant solution was kept heating at 95 °C for 5 h. The precipitate was finally collected by centrifugation, washed with deionized water and absolute ethanol for several times, and dried at 60 °C in a vacuum oven.

Preparation of CeO_2/MMNC-S-*x* Composites. The CeO_2/MMNC nanospheres and pure sulfur powder were mixed and ground in an agate mortar for about 30 min. Then, the mixture was transferred into an autoclave and heated at 155 °C for 12 h. After cooling down to room temperature naturally, the product was annealed in a tube furnace at 250 °C for 1 h to eliminate the possible sulfur particles attached on the surface of CeO_2/MMNC nanospheres. The obtained

DOI: 10.1021/acsnano.7b03227
ACS Nano 2017, 11, 7274−7283

samples were denoted as CeO_2/MMNC-S-x (x = 60%, 70%, or 80%, where x represents the initial weight ratio of sulfur in the composites).

As control samples, MMNC-S-x composites were prepared with the procedure similar to those of CeO_2/MMNC-S-x composites, except for the CeO_2/MMNC nanospheres which were replaced by pristine MMNC nanospheres.

Characterizations. Scanning electron microscopy (SEM) images and energy dispersive X-ray spectroscopy (EDX) profiles were collected on a JEOL JSM-6480 instrument. Transmission electron microscopy (TEM, JEM-2100), scanning TEM (STEM) images, and energy-filtered TEM (EFTEM) elemental mapping were taken on a JEOL JEM-2100F using an accelerating voltage of 200 kV. The powder X-ray diffraction (XRD) patterns were recorded with an X-ray diffractometer (Bruker D-8 Advance) using Cu Kα (λ = 1.5406 Å) radiation at a scanning rate of 6° min^{-1}. Raman analysis was performed on a Horiba JY Raman spectrometer using a 473 nm laser source. N_2 adsorption−desorption isotherms were obtained through Brunauer−Emmett−Teller (BET) method at 77 K on a Quantachrome Autosorb-IQ-2C-TCD-VP instrument. X-ray photoelectron spectra (XPS) were performed on a PHI-5000 VersaProbe X-ray photoelectron spectrometer using an Al Kα X-ray radiation. Thermogravimetric analysis (TGA) was performed on a NETZSCH STA 449C instrument under N_2 atmosphere from room temperature to 600 °C at a heating rate of 10 °C min^{-1}.

Electrochemical Measurements. The sulfur composite cathodes were prepared by mixing the selected samples, acetylene black and binder (polyvinylidene fluoride, PVDF) in *N*-methy-pyrrolidinone (NMP) solvent with a weight ratio of 80:10:10. The mixture was stirred for 24 h, spread on an aluminum foil, and then dried in a vacuum oven at 60 °C to remove the solvent. The Li−S batteries were assembled in an argon-filled glovebox with the above-prepared sulfur composite cathodes and lithium metal foil anodes. A solution of 1.0 M bis(trifluoro-methane)sulfonamide lithium (LiTFSI) dissolved in a mixed solvent of 1,2-dimethoxyethane (DME) and 1,3-dioxolane (DOL) with a 1:1 volume ratio containing $LiNO_3$ (1 wt %) was used as the electrolyte, and 15 μL of electrolyte was used in the coin cells. The cycling performances of Li−S cells were measured on a LAND CT2001A analyzer at different current densities with a potential window of 1.7−2.8 V vs Li/Li^+. The CV curves were collected on a Chenhua CHI-760 electrochemical workstation at a scan rate of 0.2 mV s^{-1} between 1.8 and 2.7 V. EIS analysis was carried out in the range from 100 kHz to 0.01 Hz. The assembly of soft-packaged Li−S batteries was similar to that of coin cells. The sulfur composite cathode (~24 cm^2 in area, sulfur loading is 3.8 mg cm^{-2}) was stacked and assembled into a soft-package Li−S battery against Li anodes with the same electrolyte used in coin cells. The specific capacities were calculated based on the loading weight of sulfur.

Computational Method. Density functional theory (DFT) was employed to calculate the binding energy (E_b) between the substrate and the polysulfides, which is defined by

$$E_{ads} = E_{s+sub} - E_s - E_{sub}$$

where E_{s+sub}, E_s, and E_{sub} are the energy of the polysulfides-substrate, polysulfides, and substrate, respectively. The initial conformation of all molecules was obtained by molecular mechanics (MM) method (Forcite module). The DFT calculations were performed in the Dmol3 module of Accelrys Material Studio. The exchange−correlation functional was approximated by the Perdew−Burke−Ernzerhof (PBE) method. The DFT semicore pseudopotentials were used to calculate the core−electron interactions. The DFT-D (D stands for dispersion) approach with the Ortmann−Bechstedt−Schmidt (OBS) vdW correction was used to accurately describe the vdW interactions, which influence the adsorption configurations of Li_2S_x species on substrates. The solvation effect was considered by the COSMO model with a dielectric constant of 6.18 to mimic the mixed DME/DOL solvent.

ASSOCIATED CONTENT

Supporting Information

The Supporting Information is available free of charge on the ACS Publications website at DOI: 10.1021/acsnano.7b03227.

Table S1, Figures S1−S19, and references (PDF)

AUTHOR INFORMATION

Corresponding Author

*E-mail: zhongjin@nju.edu.cn.

ORCID

Tao Chen: 0000-0003-2536-4145

Jie Liu: 0000-0003-0451-6111

Zhong Jin: 0000-0001-8860-8579

Notes

The authors declare no competing financial interest.

ACKNOWLEDGMENTS

This work is supported by National Key Research and Development Program of China (2017YFA0208200, 2016YFB0700600), National Key Basic Research Program (2015CB659300), Projects of NSFC (21403105, 21573108), China Postdoctoral Science Foundation (2015M581769), Natural Science Foundation of Jiangsu Province for Young Scholars (BK20160647 and BK20150583), Fundamental Research Funds for the Central Universities (020514380107), and a project funded by the Priority Academic Program Development of Jiangsu Higher Education Institutions.

REFERENCES

(1) Dunn, B.; Kamath, H.; Tarascon, J. M. Electrical Energy Storage for the Grid: a Battery of Choices. *Science* **2011**, *334*, 928−935.

(2) Simon, P.; Gogotsi, Y. Materials for Electrochemical Capacitors. *Nat. Mater.* **2008**, *7*, 845−854.

(3) Arico, A. S.; Bruce, P.; Scrosati, B.; Tarascon, J.; van Schalkwijk, W. Nanostructured Materials for Advanced Energy Conversion and Storage Devices. *Nat. Mater.* **2005**, *4*, 366−377.

(4) Bruce, P. G.; Scrosati, B.; Tarascon, J. Nanomaterials for Rechargeable Lithium Batteries. *Angew. Chem., Int. Ed.* **2008**, *47*, 2930−2946.

(5) Wang, Y. R.; Chen, R. P.; Chen, T.; Lv, H. L.; Zhu, G. Y.; Ma, L. B.; Wang, C. X.; Jin, Z.; Liu, J. Emerging Non-Lithium Ion Batteries. *Energy Storage Mater.* **2016**, *4*, 103−129.

(6) Qiu, Y.; Li, W. F.; Zhao, W.; Li, G. Z.; Hou, Y.; Liu, M. N.; Zhou, L. S.; Ye, F. M.; Li, H. F.; Wei, Z. H.; Yang, S. H.; Duan, W. H.; Ye, Y. F.; Guo, J. H.; Zhang, Y. G. High-Rate, Ultralong Cycle-Life Lithium/Sulfur Batteries Enabled by Nitrogen-Doped Graphene. *Nano Lett.* **2014**, *14*, 4821−4827.

(7) Manthiram, A.; Fu, Y. Z.; Su, Y. S. Challenges and Prospects of Lithium-Sulfur Batteries. *Acc. Chem. Res.* **2013**, *46*, 1125−1134.

(8) Seh, Z. W.; Sun, Y. M.; Zhang, Q. F.; Cui, Y. Designing High-Energy Lithium−Sulfur Batteries. *Chem. Soc. Rev.* **2016**, *45*, 5605−5634.

(9) Bruce, P. G.; Freunberger, S. A.; Hardwick, L. J.; Tarascon, J. M. Li-O_2 and Li-S Batteries with High Energy Storage. *Nat. Mater.* **2012**, *11*, 19−29.

(10) Yin, Y. X.; Xin, S.; Guo, Y. G.; Wan, L. J. Lithium-Sulfur Batteries: Electrochemistry, Materials, and Prospects. *Angew. Chem., Int. Ed.* **2013**, *52*, 13186−13200.

(11) Hassoun, J.; Scrosati, B. A High-Performance Polymer Tin Sulfur Lithium Ion Battery. *Angew. Chem., Int. Ed.* **2010**, *49*, 2371−2374.

(12) Yang, Y.; Zheng, G.; Cui, Y. Nanostructured Sulfur Cathodes. *Chem. Soc. Rev.* **2013**, *42*, 3018−3032.

DOI: 10.1021/acsnano.7b03227
ACS Nano 2017, 11, 7274−7283

(13) Wang, L.; Dong, Z. H.; Wang, D.; Zhang, F. X.; Jin, J. Covalent Bond Glued Sulfur Nanosheet-Based Cathode Integration for Long-Cycle-Life Li-S Batteries. *Nano Lett.* **2013**, *13*, 6244−6250.
(14) Lyu, Z. Y.; Xu, D.; Yang, L. J.; Che, R. C.; Feng, R.; Zhao, J.; Li, Y.; Wu, Q.; Wang, X. Z.; Hu, Z. Hierarchical Carbon Nanocages Confining High-Loading Sulfur for High-Rate Lithium-Sulfur Batteries. *Nano Energy* **2015**, *12*, 657−665.
(15) Schuster, J.; He, G.; Mandlmeier, B.; Yim, T.; Lee, K. T.; Bein, T.; Nazar, L. F. Spherical Ordered Mesoporous Carbon Nanoparticles with High Porosity for Lithium-Sulfur Batteries. *Angew. Chem., Int. Ed.* **2012**, *51*, 3591−3595.
(16) Chen, R. J.; Zhao, T.; Lu, J.; Wu, F.; Li, L.; Chen, J. Z.; Tan, G. Q.; Ye, Y. S.; Amine, K. Graphene-Based Three-Dimensional Hierarchical Sandwich-Type Architecture for High-Performance Li/S Batteries. *Nano Lett.* **2013**, *13*, 4642−4649.
(17) Lu, S. T.; Cheng, Y. W.; Wu, X. H.; Liu, J. Significantly Improved Long-Cycle Stability in High-Rate Li-S Batteries Enabled by Coaxial Graphene Wrapping Over Sulfur-Coated Carbon Nanofibers. *Nano Lett.* **2013**, *13*, 2485−2489.
(18) Ji, X.; Lee, K. T.; Nazar, L. F. A Highly Ordered Nanostructured Carbon-Sulphur Cathode for Lithium-Sulphur Batteries. *Nat. Mater.* **2009**, *8*, 500−506.
(19) Ding, Y. L.; Kopold, P.; Hahn, K.; van Aken, P. A.; Maier, J.; Yu, Y. Facile Solid-State Growth of 3D Well-Interconnected Nitrogen-Rich Carbon Nanotube-Graphene Hybrid Architectures for Lithium-Sulfur Batteries. *Adv. Funct. Mater.* **2016**, *26*, 1112−1119.
(20) Song, J.; Xu, T.; Gordin, M. L.; Zhu, P.; Lv, D.; Jiang, Y. B.; Chen, Y.; Duan, Y.; Wang, D. Nitrogen-Doped Mesoporous Carbon Promoted Chemical Adsorption of Sulfur and Fabrication of High-Areal-Capacity Sulfur Cathode with Exceptional Cycling Stability for Lithium-Sulfur Batteries. *Adv. Funct. Mater.* **2014**, *24*, 1243−1250.
(21) Song, J.; Gordin, M. L.; Xu, T.; Chen, S.; Yu, Z.; Sohn, H.; Lu, J.; Ren, Y.; Duan, Y.; Wang, D. Strong Lithium Polysulfide Chemisorption on Electroactive Sites of Nitrogen-Doped Carbon Composites for High-Performance Lithium-Sulfur Battery Cathodes. *Angew. Chem., Int. Ed.* **2015**, *54*, 4325−4329.
(22) Tang, C.; Zhang, Q.; Zhao, M. Q.; Huang, J. Q.; Cheng, X. B.; Tian, G. L.; Peng, H. J.; Wei, F. Nitrogen-Doped Aligned Carbon Nanotube/Graphene Sandwiches: Facile Catalytic Growth on Bifunctional Natural Catalysts and Their Applications as Scaffolds for High-Rate Lithium-Sulfur Batteries. *Adv. Mater.* **2014**, *26*, 6100−6105.
(23) Seh, Z. W.; Wang, H. T.; Hsu, P. C.; Zhang, Q. F.; Li, W. Y.; Zheng, G. Y.; Yao, H. B.; Cui, Y. Facile Synthesis of Li_2S-Polypyrrole Composite Structures for High-Performance Li_2S Cathodes. *Energy Environ. Sci.* **2014**, *7*, 672−676.
(24) Liang, Z.; Zheng, G.; Li, W.; Seh, Z. W.; Yao, H.; Yan, K.; Kong, D.; Cui, Y. Sulfur Cathodes with Hydrogen Reduced Titanium Dioxide Inverse Opal Structure. *ACS Nano* **2014**, *8*, 5249−5256.
(25) Tao, X.; Wang, J.; Ying, Z.; Cai, Q.; Zheng, G.; Gan, Y.; Huang, H.; Xia, Y.; Liang, C.; Zhang, W.; Cui, Y. Strong Sulfur Binding with Conducting Magnéli-Phase Ti_nO_{2n-1} Nanomaterials for Improving Lithium-Sulfur Batteries. *Nano Lett.* **2014**, *14*, 5288−5294.
(26) Zhang, S.; Tran, D. T. Pyrite FeS_2 as an Efficient Adsorbent of Lithium Polysulphide for Improved Lithium−Sulphur Batteries. *J. Mater. Chem. A* **2016**, *4*, 4371−4374.
(27) Ma, L.; Wei, S.; Zhuang, H. L.; Hendrickson, K. E.; Hennig, R. G.; Archer, L. A. Hybrid Cathode Architectures for Lithium Batteries Based on TiS_2 and Sulfur. *J. Mater. Chem. A* **2015**, *3*, 19857−19866.
(28) Zheng, J.; Tian, J.; Wu, D.; Gu, M.; Xu, W.; Wang, C.; Gao, F.; Engelhard, M. H.; Zhang, J. G.; Liu, J.; Xiao, J. Lewis Acid-Base Interactions Between Polysulfides and Metal Organic Framework in Lithium Sulfur Batteries. *Nano Lett.* **2014**, *14*, 2345−2352.
(29) Zhou, J. W.; Li, R.; Fan, X. X.; Chen, Y. F.; Han, R. D.; Li, W.; Zheng, J.; Wang, B.; Li, X. G. Rational Design of a Metal-Organic Framework Host for Sulfur Storage in Fast, Long-Cycle Li-S Batteries. *Energy Environ. Sci.* **2014**, *7*, 2715−2724.
(30) Hart, C. J.; Cuisinier, M.; Liang, X.; Kundu, D.; Garsuch, A.; Nazar, L. F. Rational Design of Sulphur Host Materials for Li-S Batteries: Correlating Lithium Polysulphide Adsorptivity and Self-Discharge Capacity Loss. *Chem. Commun.* **2015**, *51*, 2308−2311.
(31) Tao, Y. Q.; Wei, Y. J.; Liu, Y.; Wang, J. T.; Qiao, W. M.; Ling, L. C.; Long, D. H. Kinetically-Enhanced Polysulfide Redox Reactions by Nb_2O_5 Nanocrystals for High-Rate Lithium-Sulfur Battery. *Energy Environ. Sci.* **2016**, *9*, 3230−3239.
(32) Li, Y. J.; Fan, J. M.; Zheng, M. S.; Dong, Q. F. A Novel Synergistic Composite with Multi-Functional Effects for High-Performance Li-S Batteries. *Energy Environ. Sci.* **2016**, *9*, 1998−2004.
(33) Yuan, Z.; Peng, H. J.; Hou, T. Z.; Huang, J. Q.; Chen, C. M.; Wang, D. W.; Cheng, X. B.; Wei, F.; Zhang, Q. Powering Lithium-Sulfur Battery Performance by Propelling Polysulfide Redox at Sulfiphilic Hosts. *Nano Lett.* **2016**, *16*, 519−527.
(34) Qian, X. Y.; Jin, L. N.; Zhu, L.; Yao, S. S.; Rao, D. W.; Shen, X. Q.; Xi, X. M.; Xiao, K. S.; Qin, S. B. CeO_2 Nanodots Decorated Ketjen Black for High Performance Lithium-Sulfur Batteries. *RSC Adv.* **2016**, *6*, 111190−111196.
(35) Carter, R.; Oakes, L.; Muralidharan, N.; Cohn, A. P.; Douglas, A.; Pint, C. L. Deposition of V_2O_5 and Sulfur-Filled Carbon Nanotubes for Lithium-Sulfur Batteries. *ACS Appl. Mater. Interfaces* **2017**, *9*, 7185−7192.
(36) Wang, X. L.; Li, G.; Li, J. D.; Zhang, Y. N.; Wook, A.; Yu, A. P.; Chen, Z. W. Structural and Chemical Synergistic Encapsulation of Polysulfides Enables Ultralong-Life Lithium-Sulfur Batteries. *Energy Environ. Sci.* **2016**, *9*, 2533−2538.
(37) Han, X. G.; Xu, Y. H.; Chen, X. Y.; Chen, Y. C.; Weadock, N.; Wan, J. Y.; Zhu, H. L.; Liu, Y. L.; Li, H. Q.; Rubloff, G.; Wang, C. S.; Hu, L. B. Reactivation of Dissolved Polysulfides in Li-S Batteries Based on Atomic Layer Deposition of Al_2O_3 in Nanoporous Carbon Cloth. *Nano Energy* **2013**, *2*, 1197−1206.
(38) Li, Z.; Zhang, J. T.; Lou, X. W. Hollow Carbon Nanofibers Filled with MnO_2 Nanosheets as Efficient Sulfur Hosts for Lithium-Sulfur Batteries. *Angew. Chem., Int. Ed.* **2015**, *54*, 12886−12890.
(39) Zhang, Q. F.; Wang, Y. P.; Seh, Z. W.; Fu, Z. H.; Zhang, R. F.; Cui, Y. Understanding the Anchoring Effect of Two-Dimensional Layered Materials for Lithium-Sulfur Batteries. *Nano Lett.* **2015**, *15*, 3780−3786.
(40) An, Y. L.; Zhang, Z.; Fei, H. F.; Xiong, S. L.; Ji, B.; Feng, J. K. Ultrafine TiO_2 Confined in Porous-Nitrogen-Doped Carbon from Metal-Organic Frameworks for High-Performance Lithium-Sulfur Batteries. *ACS Appl. Mater. Interfaces* **2017**, *9*, 12400−12407.
(41) Zheng, C.; Niu, S. Z.; Lv, W.; Zhou, G. M.; Li, J.; Fan, S. X.; Deng, Y. Q.; Pan, Z. Z.; Li, B. H.; Kang, F. Y.; Yang, Q. H. Propelling Polysulfides Transformation for High-Rate and Long-Life Lithium-Sulfur Batteries. *Nano Energy* **2017**, *33*, 306−312.
(42) Rehman, S.; Tang, T. Y.; Ali, Z.; Huang, X. X.; Hou, Y. L. Integrated Design of MnO_2@Carbon Hollow Nanoboxes to Synergistically Encapsulate Polysulfides for Empowering Lithium Sulfur Batteries. *Small* **2017**, *13*, 1700087.
(43) Liang, X.; Kwok, C. Y.; Lodi-Marzano, F.; Pang, Q.; Cuisinier, M.; Huang, H.; Hart, C. J.; Houtarde, D.; Kaup, K.; Sommer, H.; Brezesinski, T.; Janek, J.; Nazar, L. F. Tuning Transition Metal Oxide-Sulfur Interactions for Long Life Lithium Sulfur Batteries: the "Goldilocks" Principle. *Adv. Energy Mater.* **2016**, *6*, 1501636.
(44) Yu, T.; Lim, B.; Xia, Y. N. Aqueous-Phase Synthesis of Single-Crystal Ceria Nanosheets. *Angew. Chem., Int. Ed.* **2010**, *49*, 4484−4487.
(45) Gu, H.; Soucek, M. D. Preparation and Characterization of Monodisperse Cerium Oxide Nanoparticles in Hydrocarbon Solvents. *Chem. Mater.* **2007**, *19*, 1103−1110.
(46) Zheng, F. C.; Yang, Y.; Chen, Q. W. High Lithium Anodic Performance of Highly Nitrogen-Doped Porous Carbon Prepared from A Metal-Organic Framework. *Nat. Commun.* **2014**, *5*, 5261.
(47) Peng, H. J.; Zhang, Q. Designing Host Materials for Sulfur Cathodes: from Physical Confinement to Surface Chemistry. *Angew. Chem., Int. Ed.* **2015**, *54*, 11018−11020.
(48) Yang, J.; Xie, J.; Zhou, X. Y.; Zou, Y. L.; Tang, J. J.; Wang, S. C.; Chen, F.; Wang, L. Y. Functionalized N-Doped Porous Carbon

DOI: 10.1021/acsnano.7b03227
ACS Nano 2017, 11, 7274−7283

Nanofiber Webs for a Lithium-Sulfur Battery with High Capacity and Rate Performance. *J. Phys. Chem. C* **2014**, *118*, 1800−1807.
(49) Beche, E.; Charvin, P.; Perarnau, D.; Abanades, S.; Flamant, G. Ce 3d XPS Investigation of Cerium Oxides and Mixed Cerium Oxide ($Ce_xTi_yO_z$). *Surf. Interface Anal.* **2008**, *40*, 264−267.
(50) Zhou, G. M.; Zhao, Y. B.; Manthiram, A. Dual-Confined Flexible Sulfur Cathodes Encapsulated in Nitrogen-Doped Double-Shelled Hollow Carbon Spheres and Wrapped with Graphene for Li-S Batteries. *Adv. Energy Mater.* **2015**, *5*, 1402263.
(51) Su, Y. S.; Manthiram, A. Lithium-Sulphur Batteries with a Microporous Carbon Paper as a Bifunctional Interlayer. *Nat. Commun.* **2012**, *3*, 1166.
(52) Zhao, Y.; Wu, W.; Li, J.; Xu, Z.; Guan, L. Encapsulating MWCNTs into Hollow Porous Carbon Nanotubes: a Tube-in-Tube Carbon Nanostructure for High-Performance Lithium-Sulfur Batteries. *Adv. Mater.* **2014**, *26*, 5113−5118.
(53) Xu, R.; Lu, J.; Amine, K. Progress in Mechanistic Understanding and Characterization Techniques of Li-S Batteries. *Adv. Energy Mater.* **2015**, *5*, 1500408.
(54) Li, Z. Q.; Li, C. X.; Ge, X. L.; Ma, J. Y.; Zhang, Z. W.; Li, Q.; Wang, C. X.; Yin, L. W. Reduced Graphene Oxide Wrapped MOFs-Derived Cobalt-Doped Porous Carbon Polyhedrons as Sulfur Immobilizers as Cathodes for High Performance Lithium Sulfur Batteries. *Nano Energy* **2016**, *23*, 15−26.
(55) Kong, W. B.; Yan, L. J.; Luo, Y. F.; Wang, D. T.; Jiang, K. L.; Li, Q. Q.; Fan, S. S.; Wang, J. P. Ultrathin MnO_2/Graphene Oxide/Carbon Nanotube Interlayer as Efficient Polysulfide-Trapping Shield for High-Performance Li-S Batteries. *Adv. Funct. Mater.* **2017**, *27*, 1606663.
(56) Pang, Q.; Kundu, D. P.; Cuisinier, M.; Nazar, L. F. Surface-Enhanced Redox Chemistry of Polysulfides on a Metallic and Polar Host for Lithium-Sulphur Batteries. *Nat. Commun.* **2014**, *5*, 4759.
(57) Sun, Z. H.; Zhang, J. Q.; Yin, L. C.; Hu, G. J.; Fang, R. P.; Cheng, H. M.; Li, F. Conductive Porous Vanadium Nitride/Graphene Composite as Chemical Anchor of Polysulfides for Lithium-Sulfur Batteries. *Nat. Commun.* **2017**, *8*, 14627.

DOI: 10.1021/acsnano.7b03227
ACS Nano 2017, 11, 7274−7283